Journal of
Marine Science and Engineering

MDPI

Article

CCTV-Based Quantification of Remaining Beach Width Associated with Wave Runup on a Sandy Beach

Bohyeon Hwang [1,*], Minsuk Shin [1], Guenam Kim [1] and Kihyon Kim [2]

[1] Department of Coastal Management, GeoSystem Research Corp., Gunpo 15807, Republic of Korea
[2] GeoSystem Research Corp., Gunpo 15807, Republic of Korea
* Correspondence: zpzpxpxp@naver.com; Tel.: +82-10-8991-1349

Abstract

Wave runup reduces the horizontal beach buffer. At Namho Beach, South Korea, orthorectified CCTV estimation of Remaining Beach Width (RBW) and Stockdon-derived RBW sensitivity to morphology timing were evaluated separately. Sixty 10 min CCTV observation periods along two transects were analyzed. CCTV-derived P_2 RBW is a horizontal lower-tail statistic, whereas Stockdon $R_{2\%}$ is a vertical exceedance elevation converted to horizontal RBW; thus Stockdon-derived RBW was treated as an empirical comparator. ADCP wave heights at 24 m depth were reverse-shoaled to deep-water equivalents. Inter-analyst reproducibility was high (120 paired trajectories; RMSE = 0.83 m; $r = 0.994$). In the screened Q_{95} cohort, association was moderate with an appreciable error at Transect 1 ($n = 35$, $r = 0.66$, RMSE = 5.55 m, NSE = 0.18) and weak at Transect 2 ($n = 35$, $r = 0.24$, RMSE = 4.53 m, NSE = -0.44). Survey-matched agreement was stronger ($n = 25$ per transect; r = 0.89–0.90; RMSE = 2.62–3.53 m; NSE = 0.58–0.65). In the selected morphology-input sensitivity set, the absolute CCTV–Stockdon difference was descriptively 1.94 m smaller with the nearest morphology; contrasts were negative in 21 of 27 periods and four of five survey epochs. CCTV provided time-resolved RBW observations, but agreement was dataset- and transect-dependent.

Keywords: remaining beach width; wave runup; coastal video monitoring; Stockdon runup parameterization; beach morphology; orthorectification; timestack analysis

1. Introduction

Coastal zones are increasingly exposed to wave-driven hazards associated with storms, extreme water levels, and long-term sea-level rise. Among the nearshore processes controlling these hazards, wave runup is particularly important because it represents the landward excursion of wave uprush and determines whether wave-induced water levels remain confined to the foreshore or reach dunes, coastal structures, and backshore areas. The elevation of runup relative to coastal morphology has been used to classify storm impacts into swash, collision, overwash, and inundation regimes, indicating that coastal response is governed by both hydrodynamic forcing and beach–backshore geometry [1]. In coastal engineering practice, wave overtopping is also recognized as a principal mechanism of flood risk at sea defenses and shoreline structures, and its reduction is a key requirement for the design, management, and adaptation of coastal infrastructure [2]. Wave runup further contributes to total water levels through wave setup and swash motions and has been identified as a major driver of beach and foredune erosion during storm events [3,4]. Accordingly, accurate estimation of runup is required for assessing storm-wave, surge,

Check for updates

Academic Editor: Isavela N. Monioudi

Received: 30 June 2026
Revised: 25 July 2026
Accepted: 28 July 2026
Published: 29 July 2026

tsunami, erosion, overtopping, and beach-flooding hazards [5,6]. However, the practical assessment of such hazards remains challenging because the landward extent of wave action depends on the combined effects of offshore waves, water levels, beach morphology, and time-varying swash processes. These considerations indicate that coastal risk cannot be evaluated solely from vertical runup elevation; horizontal indicators describing the remaining beach buffer are also required.

Empirical runup formulations have been widely used because runup-related water levels can be estimated from a limited set of hydrodynamic and morphological inputs [1–4,6]. Among these formulations, the formulation proposed by Stockdon et al. [3] remains one of the most widely used predictors for natural sandy beaches. In that formulation, the 2% exceedance runup elevation, $R_{2\%}$, is parameterized using offshore wave height, deep-water wavelength, and foreshore beach slope through separate representations of wave setup and swash. This empirical approach has been incorporated into operational total-water-level and coastal-change forecasting systems, where wave runup is combined with tides and surge to evaluate erosion, overwash, and inundation hazards [7,8]. Empirical runup estimates have also been applied to coastal flood mapping, field-debris-based flood assessment, and video-supported coastal vulnerability studies, demonstrating their practical value for local- to regional-scale hazard applications [5,6,9]. Nevertheless, their reliability depends strongly on the representativeness of the morphological parameters used in the calculation. On natural beaches, defining a single representative beach slope is inherently difficult because profiles are commonly non-planar and temporally variable [3]. Field observations have also shown that runup can vary substantially alongshore in response to local foreshore slope and morphology [10], while spatial and temporal variability in beach slope can produce differences on the order of 1 m in predicted wave-induced water levels [11]. Recent studies have therefore extended empirical approaches by considering additional morphological controls, including berm or dry beach width [12], sediment type and grain size on gravel beaches [13], and surf-zone slope, wave angle, and directional spreading in model-derived formulations [14]. These findings indicate that empirical runup formulas are useful for hazard assessment, but their conversion into horizontal exposure metrics such as Remaining Beach Width requires temporally representative and site-specific beach morphology. Accordingly, when Stockdon $R_{2\%}$ is converted to horizontal RBW, the resulting value should be interpreted as an empirical comparator conditioned on wave input, water level, surveyed beach-profile geometry, and the horizontal-conversion assumptions, rather than as an absolute validation target.

Coastal video monitoring has become an effective remote-sensing approach for observing nearshore morphology, shoreline motion, and swash-zone processes at temporal scales that are difficult to achieve with conventional field surveys. Early video-based studies showed that time-exposure and timestack images could be used to extract quantitative information on surf-zone morphology and shoreline variability, and the Argus system subsequently provided a technical basis for long-term optical monitoring of the nearshore environment [15,16]. For wave runup applications, timestack analysis has been widely adopted because the time-varying landward waterline or swash extrema can be tracked along cross-shore transects. Salmon et al. [4] used video-derived timestacks to digitize maximum swash excursions and obtain runup time series during storm events, while Vousdoukas et al. [5] combined coastal video imagery with topographic surveys to extract $R_{2\%}$ values and assess coastal vulnerability at a mesotidal beach. Video-derived coastal state indicators, including shoreline position, intertidal beach volume, and storm-response indicators, have also been proposed to support coastal management [17]. More recent studies have improved the automation and robustness of runup extraction using Radon-transform-based motion detection [18], machine-learning-based total-water-level extraction [19], and

https://doi.org/10.3390/jmse14151398

coastal CCTV cameras for automated tsunami runup monitoring [20]. However, these studies have mainly focused on vertical runup elevation, total water level, shoreline position, or event detection, whereas fewer studies have used video-observed whitewater excursion to quantify the time-varying horizontal beach buffer remaining during energetic conditions.

Despite these advances, a methodological gap remains in translating runup observations and empirical runup estimates into a management-oriented horizontal exposure metric. Previous studies have demonstrated that video imagery can measure swash extrema, runup elevation, total water level, and shoreline variability, and that empirical formulas can provide practical estimates of runup-related hazard levels [4–6,15–20]. However, coastal managers often need to evaluate not only how high wave uprush reaches, but also how much horizontal beach buffer remains between the active wave-affected zone and a predefined landward reference, such as a coastal baseline, dune toe, seawall, or coastal road. This residual horizontal buffer is particularly important on narrow or rapidly changing beaches, where small variations in beach width or foreshore slope can substantially alter the apparent level of exposure. In this study, Remaining Beach Width (RBW) is defined as the horizontal distance between a predefined coastal baseline and the landward limit of visually identifiable wave-induced whitewater observed along a fixed cross-shore transect. Although RBW can be inferred from either direct video observations or empirical runup calculations converted into horizontal excursion, few studies have explicitly quantified CCTV-derived RBW and compared it with Stockdon-derived RBW under energetic wave conditions. Moreover, the effect of temporal mismatch between continuous CCTV observations and intermittently surveyed beach morphology has not been sufficiently examined for RBW estimation.

Two related but distinct objectives were addressed. First, orthorectified coastal CCTV imagery was evaluated as a time-resolved observational method for estimating horizontal RBW, with Stockdon-derived RBW used only as an empirical comparator rather than as an absolute validation target. Second, the sensitivity of Stockdon-derived RBW to the temporal representativeness of intermittently surveyed beach-profile morphology was quantified by recalculating the same CCTV observation periods under alternative morphology inputs. These objectives were evaluated separately so that differences between non-identical datasets were not attributed solely to morphology timing.

2. Materials and Methods

2.1. Study Site and Monitoring Configuration

Namho Beach, located in Yeongdeok-gun, Gyeongsangbuk-do, on the eastern coast of South Korea, was selected as the study site. The beach is an arc-shaped sandy shoreline approximately 1154 m long, with beach widths ranging from 6 to 33 m. The shoreline extends from approximately 36°20′00″ N, 129°22′46″ E to 36°19′25″ N, 129°22′53″ E. Namho Beach is monitored under a local-government coastal-erosion monitoring program, in which terrestrial beach-profile surveys are conducted four times per year. Nominally continuous 24 h CCTV imagery is also available, although intermittent gaps occur in the archive. Offshore wave conditions were measured using a Signature 500 acoustic Doppler current profiler (ADCP; Nortek AS, Rud, Norway), installed approximately 1.2 km offshore from the study area at a water depth of approximately 24 m. The instrument recorded significant wave height H_{m0}, peak wave period T_p, and peak wave direction θ_p at 1 h intervals. All spatial data were referenced to Korea TM East Belt 2010 (EPSG:5187), and elevations were referenced to Incheon Mean Sea Level (IMSL; 26.6871 m). Nine cross-shore survey lines are maintained for terrestrial beach-profile surveys. Among them, Line 5 and Line 6 were selected for CCTV analysis and are hereafter referred to as Transect 1 and Transect 2, respectively. These transects were selected because the coastal baseline, shoreline, and active swash zone were clearly visible within the CCTV field of view, and their relatively short distances from the camera helped reduce perspective-related distortion during orthorectification. The median sediment diameters D_{50} at Transects 1 and 2 were 0.57 and 0.42 mm, respectively. The coastal baseline was defined as the landward reference line separating the active beach from the hinterland or adjacent coastal infrastructure. Remaining Beach Width (RBW) was measured relative to this common reference line in both the CCTV-based and empirical analyses. The locations of the coastal baseline, Transects 1 and 2, the CCTV camera, and the offshore ADCP station are shown in Figure 1. The CCTV system consisted of an XNB-8002 network box camera (Hanhwa Vision CO., Ltd., Seongnam, Republic of Korea) installed at an elevation of approximately 19.7 m. The camera recorded imagery at a spatial resolution of 3328 × 1872 pixels and a nominal frame rate of 30 or 10 fps.

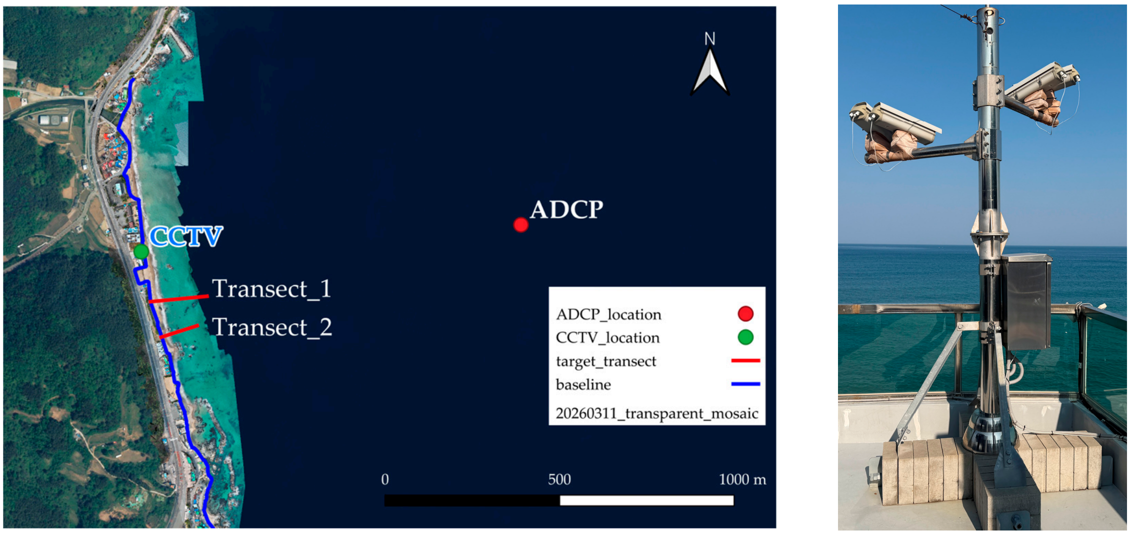

(**a**) (**b**)

Figure 1. Study site and monitoring configuration at Namho Beach, South Korea. (**a**) Orthomosaic-based site map showing the coastal baseline, Transects 1 and 2, the coastal CCTV camera, and the offshore ADCP station; (**b**) field photograph of the coastal CCTV camera system.

2.2. CCTV-Based Remaining Beach Width Extraction

CCTV-derived RBW was quantified using a custom semi-automated image-analysis workflow. The runup front was defined as the landward limit of visually identifiable wave-induced whitewater in the orthorectified images. CCTV-derived RBW was defined as the horizontal distance from the predefined coastal baseline to this front (Figure 2). The workflow comprised observation-period selection, video subsetting and frame extraction, image orthorectification, transect-based timestack generation, automated whitewater-front detection, visual quality control, manual trajectory correction, and RBW calculation in map coordinates. Frame extraction, geometric transformation, timestack construction, threshold-based segmentation, coordinate conversion, distance calculation, and output generation were automated. Every detected trajectory was visually inspected, and correction was applied only when the automated trajectory did not follow the temporally coherent landward whitewater front. The workflow was therefore classified as semi-automated; correction criteria and intervention statistics are reported in Section 2.2.4.

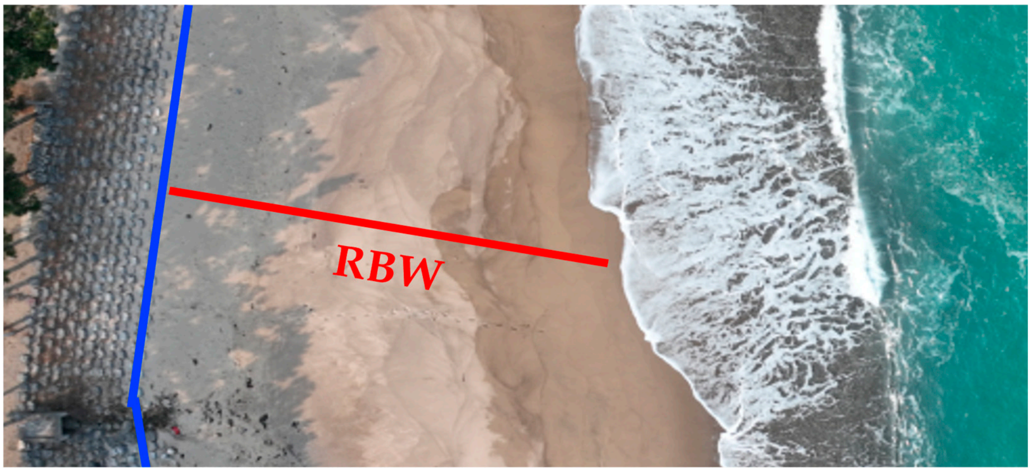

Figure 2. Conceptual definition of Remaining Beach Width (RBW) on an orthomosaic base image. The blue line denotes the coastal baseline, and the red segment denotes RBW measured from the coastal baseline to the landward runup front detected from time resolved CCTV imagery.

2.2.1. Wave-Condition Analysis, Observation-Period Selection, and Video Preparation

A reference distribution comprising 26,891 valid hourly ADCP records from 00:00 on 1 January 2023 to 09:00 on 8 April 2026 was used to define the wave-height percentiles. This hydrodynamic reference period was independent of the shorter interval for which analyzable CCTV imagery was available. Spectral significant wave height (H_{m0}), peak wave period (T_p), and peak wave direction (θ_p) were extracted after observation times had been reconstructed from the recorded date and time fields. The final CCTV dataset spanned 11 December 2023–13 March 2026. Because reliable runup-front detection required unobstructed views of the shoreline, active swash zone, coastal baseline, and both transects, only daytime imagery acquired approximately between 07:00 and 18:00 KST was considered. Each final 10 min CCTV observation period was assigned one hourly ADCP wave-reference time. The H_{m0}, T_p, and θ_p values used in the Stockdon calculation were taken from that exact hourly record; the central CCTV timestamp was no more than 29.44 min from the assigned wave-reference time. Selection was conditioned on video availability, daylight visibility, camera-view stability, field-of-view coverage, and image quality.

Two complementary analytical datasets were constructed. First, a screened high-wave cohort (hereafter, the Q_{95} cohort) was established to evaluate RBW under energetic conditions. The 95th percentile of the 1 January 2023–8 April 2026 ADCP reference distribution was used as the threshold. Potential Q_{95} observation periods were evaluated only where archived daylight CCTV imagery was available, and a period was retained only when the wave height matched to the final analyzed 10 min period equaled or exceeded this threshold:

$$H_{m0} \geq H_{m0,Q95} \tag{1}$$

The Q_{90}, Q_{95}, and Q_{99} thresholds were 1.29, 1.59, and 2.48 m, respectively (Figure 3). The analytical dataset comprised 60 selected 10 min CCTV observation periods in two non-overlapping cohorts. The Q_{95} cohort was restricted to the 35 retained periods documented in the 53-candidate screening ledger, and all 35 had matched $H_{m0} \geq 1.59$ m. The survey-matched cohort comprised five groups of five daytime observation periods associated with five beach-profile surveys. Within each group, all five periods were selected at the same local hour as the corresponding field survey: 14:00 KST for 13 December 2023, 12:00 KST for 22 April 2024, 11:00 KST for 19 February 2025, 14:00 KST for 17 April 2025, and 15:00 KST for 11 March 2026. The observation dates differed from the assigned survey dates by 0–3 calendar days. When two surveys were equally distant in calendar days, the earlier survey was used as a deterministic tie-break; this occurred on 26 March 2024, for which the 28 February and 22 April surveys were both 27 days distant. Four survey-matched periods (11, 12, and 15 December 2023 and 13 March 2026) also had matched $H_{m0} \geq 1.59$ m, but they were not reassigned post hoc to the ledger-defined Q_{95} cohort. The two cohorts therefore comprised $35 + 25 = 60$ distinct observation periods. Detailed wave-reference times and the corresponding ADCP wave conditions for all 60 selected CCTV observation periods are provied in Appendix A (Tables A1 and A2).

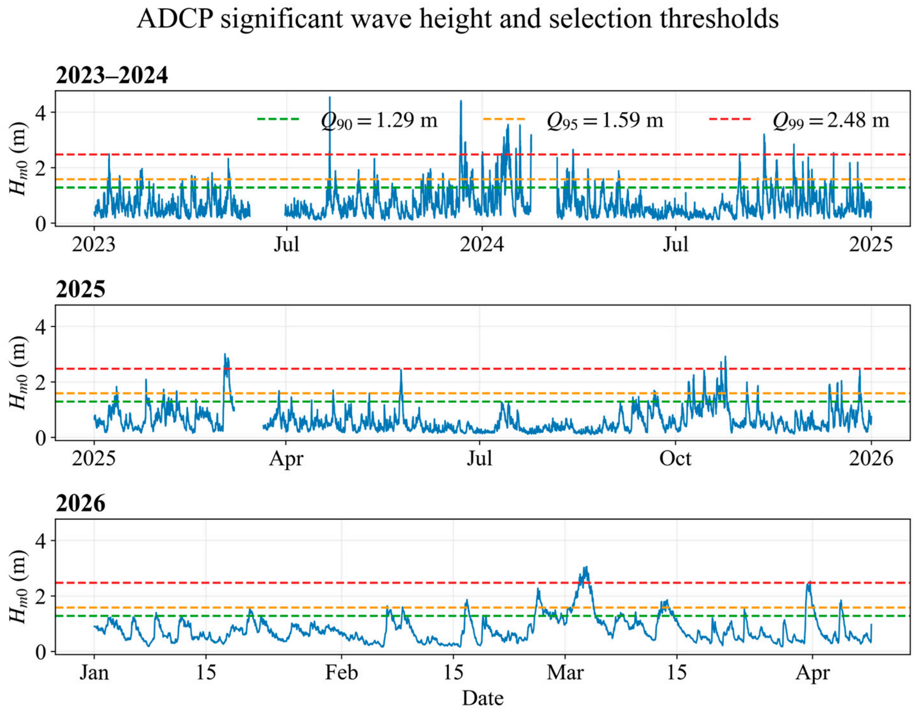

Figure 3. Hourly ADCP significant wave height from 1 January 2023 to 8 April 2026, divided into 2023–2024, 2025, and 2026 panels for readability. Dashed lines show the Q_{90}, Q_{95}, and Q_{99} thresholds calculated from the same 26,891-record reference distribution.

To evaluate sensitivity to the declustering interval, the 35 Q_{95} observation periods were grouped using 12-, 24-, and 48 h separation rules, yielding 35, 30, and 24 wave episodes, respectively. The 24 h definition was used for primary inference, while the 12- and 48 h definitions were retained as sensitivity checks.

The screening ledger documented 53 Q_{95} candidates from 16 December 2023 at 07:00 to 25 May 2025 at 07:00. Of these, 35 were retained and 18 were excluded before trajectory analysis: raw video was unavailable for 15 candidates, and night-time or low-light imagery precluded analysis for three candidates. No candidate remained unresolved. For every retained Q_{95} period, H_{m0}, T_p, and water level were matched to the final analyzed 10 min period, and all 35 matched H_{m0} values met the 1.59 m threshold. No usable CCTV video was available in the assembled archive from 26 May 2025 through 8 March 2026; that interval was outside the screened archive rather than a set of post-inspection exclusions. After the 60 selected periods entered trajectory processing, none was excluded following final visibility and orthorectification review. Each retained 10 min segment was sampled at 1 s intervals, yielding 600 frames.

2.2.2. Image Orthorectification and Geometric Assessment

The original CCTV images were acquired from an oblique viewing angle and were therefore orthorectified before timestack generation and runup-front detection. Ground control points (GCPs) distributed across the visible beach area were used to estimate the geometric relationship between image coordinates and the real-world horizontal coordinate system. Each GCP consisted of a known world coordinate (X_i, Y_i) in the adopted TM coordinate system and the corresponding image coordinate (u_i, v_i) in pixel space. The distribution of the selected GCPs is shown in Figure 4a. A planar projective transformation, or homography, was estimated between the real-world horizontal coordinate system and the CCTV image coordinate system. The inverse transformation was then used to resample the oblique CCTV image into plan-view coordinates.

$$\lambda_i \begin{bmatrix} u_i \\ v_i \\ 1 \end{bmatrix} = \mathbf{H} \begin{bmatrix} X_i \\ Y_i \\ 1 \end{bmatrix} \tag{2}$$

where $\mathbf{H}$ is the 3×3 homography matrix and λ_i is an arbitrary scale factor. The orthorectified output domain was limited to the inner portion of the transformed image containing the coastal baseline, Transects 1 and 2, the shoreline, and the active swash zone. Peripheral areas were excluded because they were more strongly affected by perspective distortion and extrapolation beyond the well-constrained GCP area. The selected output domain covered 105 m in the x-direction and 245 m in the y-direction. The orthorectified grid resolution was 0.1 m, resulting in an image size of 1051 columns and 2451 rows. Geometric performance was assessed using both in-sample GCP reprojection residuals and residuals at checkpoints withheld from homography estimation. For each evaluation point, the image coordinate was inverse-projected into the world coordinate system and compared with the measured world coordinate. The comparison between the measured world coordinates and the inverse-projected coordinates is shown in Figure 4b, providing a visual assessment of the pixel-to-world transformation consistency. Coordinate residuals were defined as:

$$e_{X,i} = \hat{X}_i - X_i, \qquad e_{Y,i} = \hat{Y}_i - Y_i, \tag{3}$$

where (X_i, Y_i) is the reference position and $(\hat{X}_i, \hat{Y}_i)$ is the reconstructed position. Root-mean-square errors were calculated as:

$$RMSE_X = \sqrt{\frac{1}{N}\sum_{i=1}^{N} e_{X,i}^2};\ RMSE_Y = \sqrt{\frac{1}{N}\sum_{i=1}^{N} e_{Y,i}^2};\ RMSE_{2D} = \sqrt{RMSE_X^2 + RMSE_Y^2} \tag{4}$$

where N is the number of evaluation points. Internal residuals were calculated from the 10 GCPs used to estimate the homography. Their mean 2D error was 1.02 m, 2D RMSE was 1.45 m, P_{95} was 2.77 m, and maximum error was 3.77 m. Because these points were used in calibration, the values were treated only as in-sample reprojection residuals and not as independent estimates of positional accuracy.

Five surveyed points withheld from homography estimation were used as independent-of-fit checkpoints. These points were surveyed in the same coordinate system but were not used to estimate the homography matrix. Their mean 2D error was 2.55 m, 2D RMSE was 3.29 m, P_{95} was 5.12 m, and maximum error was 5.55 m. A leave-one-out test using the 10 calibration GCPs yielded an RMSE of 4.30 m, which was interpreted as a measure of calibration-network sensitivity rather than as independent positional accuracy. Local geometric support was limited because only two checkpoints were located within 30 m of Transect 1 and one within 30 m of Transect 2, and the transect origins were located 7.80 and 4.40 m outside the calibration hull, respectively. The transect-resolved residuals were therefore interpreted only as empirical cross-shore checks. Projection of all five checkpoint residual vectors onto the fixed transect directions yielded cross-shore RMSE values of 0.59 m at Transect 1 and 0.21 m at Transect 2, indicating that most of the measured 2D residual was oriented alongshore. When only checkpoints within 30 m were retained, the corresponding RMSE values were 0.52 m ($n = 2$) and 0.10 m ($n = 1$), respectively; these sparse local values were not treated as stable accuracy estimates. Relief displacement associated with the sloping, time-varying beach surface could not be resolved by the planar homography; consequently, the checkpoint results did not constitute a complete error model for vertical-relief effects.

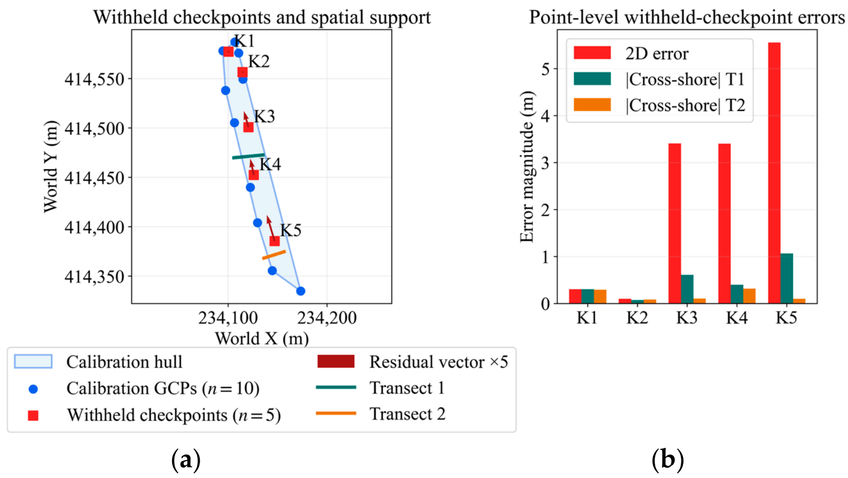

Figure 4. Independent-of-fit checkpoint assessment. (**a**) Ten calibration GCPs, five checkpoints withheld from homography estimation, the calibration hull, transects, and checkpoint residual vectors; (**b**) point-level 2D and transect-direction cross-shore residuals. The checkpoints shared the survey reference framework and were independent only of homography fitting.

2.2.3. Transect-Based Timestack Generation

Runup-front detection was performed along two fixed cross-shore transects. The resulting dataset contained 120 trajectory records: two paired transects for each of 60 CCTV observation periods. Dataset-specific summaries contained 70 Q_{95} and 50 survey-matched observation-period–transect records, with no overlap between cohorts. Each timestack covered 600 s at 1 s resolution. Image intensity was sampled along each fixed transect, normalized by row, and stacked chronologically. The horizontal axis represented cross-shore distance from the coastal baseline toward the sea, and the vertical axis represented elapsed time.

The graphical user interface (GUI) used to define frame-sampling and saved-timestack settings, load the fixed analysis transects and coastal baseline, specify the observation-period start time, and initiate transect-wise runup processing is shown in Figure 5.

2.2.4. Automatic Detection, Manual Correction, and CCTV-Derived RBW

The initial runup front was detected automatically from each transect-based timestack using a mixed grayscale–whiteness feature and row-wise Otsu thresholding [20,21]. Grayscale intensity G and an HSV-based whiteness term $W = V(1 - S)$, where V and S are normalized value and saturation, were combined as $F = 0.35G + 0.65W$ in all 240 saved analyst–transect trajectories. Within each time row, the 5th and 95th percentiles were used to normalize the feature. A dark-pixel mask, defined where both V and G were less than or equal to the stored dark threshold, was enabled in every analysis; masked samples were omitted from the row-wise Otsu calculation and removed from the candidate mask. The Otsu threshold was modified by a trajectory-specific offset and constrained to a minimum of 0.35 on the normalized feature scale. Threshold offsets were stored in 8-bit normalized-feature levels. For Analyst 1, an offset of -12 was used for 100 of 120 trajectories, with -5, 0, 2, or 24 used for the remaining 20; the dark threshold was 0.40 for 114 of 120 trajectories, with 0.16 or 0.50 used for the remaining six. For Analyst 2, offsets of −5 and −12 were used for 78 of 120 and 26 of 120 trajectories, respectively, with 0, 5, 15, 20, or 25 used for the remaining 16; the dark threshold was 0.40 for all trajectories. Otsu's method separates a feature-value distribution into two classes by maximizing the between-class variance [21]. For each time step, the optimal unadjusted threshold was determined as:

$$k_t^* = \arg\max_k \sigma_B^2(k) \tag{5}$$

$$\sigma_B^2(k) = \omega_0(k)\omega_1(k)[\mu_0(k) - \mu_1(k)]^2 \tag{6}$$

where the occurrence probabilities and class means were calculated for the two classes separated by the candidate threshold. Non-dark pixels above the adjusted threshold were classified as candidate whitewater pixels, and the landward-most candidate within the analysis region was selected at each time step. An isolated-landward-spike filter was applied within a ±3-frame neighborhood, and a centered three-point temporal median was used for 236 of 240 trajectories.

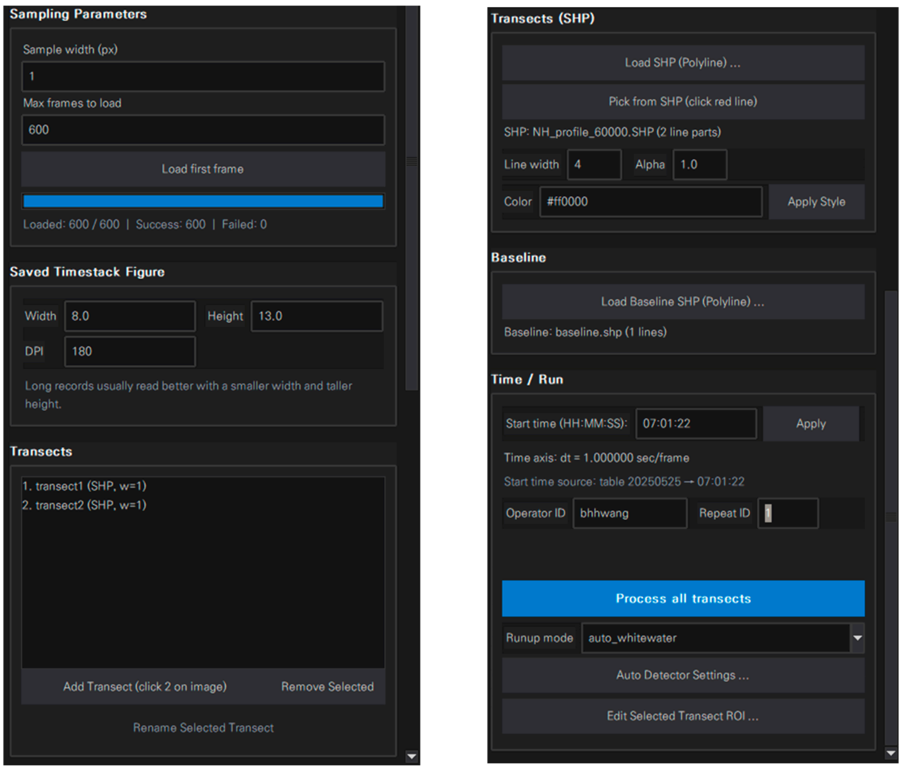

(**a**) (**b**)

Figure 5. Enlarged panels from the graphical user interface used for transect-based timestack generation and runup processing. (**a**) Frame-sampling settings, saved-timestack dimensions and resolution, and the loaded fixed analysis transects; (**b**) fixed-transect and coastal-baseline inputs, observation-period start time, operator and run metadata, and controls used to initiate transect-wise processing.

A larger spike-prominence setting and no median smoothing were used for the four Analyst 1 trajectories from 11 and 12 December 2023. The saved configurations show that local-gradient displacement, maximum-jump and median-absolute-deviation filtering, explicit gap interpolation, component opening, and dark-gap closing were not applied. For the analyst-guided correction described below, the search window and maximum temporal step were 12 and 18 pixels, respectively; fixed weights of 1.00, 0.85, 1.00, 0.25, and 8.00 were applied to the mixed feature, local edge, temporal smoothness, automatic-path prior, and analyst anchors, respectively. An example of an automatically detected trajectory retained after visual inspection is shown in Figure 6.

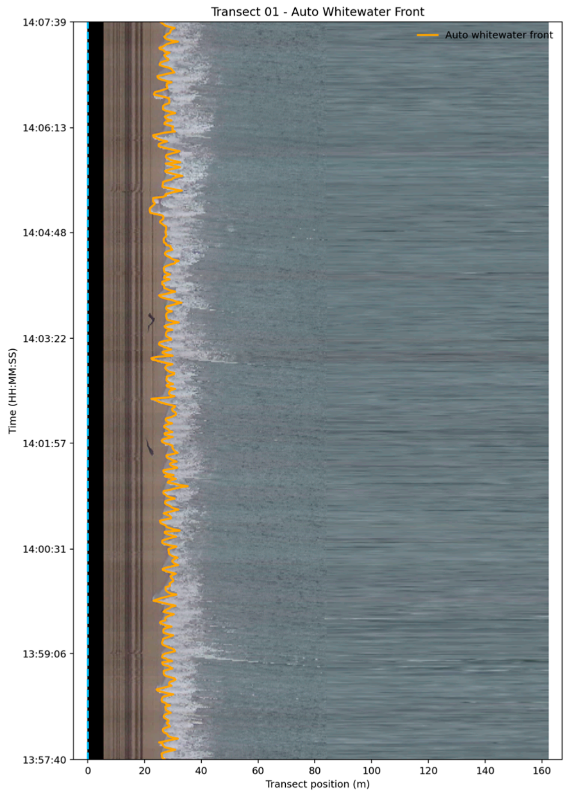

Figure 6. Example of a transect-based timestack and reviewed runup-front trajectory. The timestack was generated from orthorectified CCTV frames along a fixed cross-shore transect, and the overlay shows the automatic trajectory retained after visual inspection. No manual correction was required for this illustrative 14 December 2023 Transect 1 record.

All automatically detected trajectories were visually inspected. Manual correction was performed when the detected trajectory did not coincide with the temporally coherent landward edge of visually identifiable wave-induced whitewater. A time–distance correction region and analyst anchor points were then defined. Within that region, a constrained path was recomputed using the normalized feature, local edge strength, candidate-mask membership, a dark-pixel penalty, proximity to the original automatic path, temporal smoothness, and the analyst anchors. Only the selected segment was replaced, and the original automatic and final reviewed trajectories were retained separately. No trajectory was replaced by unconstrained frame-by-frame point picks. Because cause categories were not stored in the correction logs, correction frequency and displacement were quantified without assigning individual corrections to particular optical mechanisms. The instantaneous CCTV-derived RBW was then calculated along each transect as the horizontal distance between the coastal baseline and the detected runup front:

$$RBW_{\text{CCTV}}(t) = x_r(t) - x_B \quad (7)$$

where $x_{r(t)}$ is the cross-shore coordinate of the detected runup front at time t, x_B is the intersection of the transect with the coastal baseline, and $RBW_{(CCTV)(t)}$ is the instantaneous CCTV-derived RBW. Because both estimates use the same coastal baseline and horizontal transect coordinate system, they can be compared as horizontal beach-buffer distances; however, CCTV-derived P_2 RBW and Stockdon $R_{2\%}$ are not statistically equivalent. When the detected runup front reached or exceeded the coastal baseline, $RBW_{(CCTV)(t)}$ was set to 0 m under the non-negative RBW convention. Smaller $RBW_{(CCTV)(t)}$ values indicate more landward swash penetration and a narrower residual beach buffer. A representative near-extreme observation-period-scale value was obtained from the 2nd percentile of the instantaneous RBW series:

$$RBW_{\text{CCTV}} = P_2[RBW_{\text{CCTV}}(t)] \tag{8}$$

where P_2 denotes the 2nd percentile. This lower-tail statistic was selected as an operational summary of near-extreme landward excursion because it is less sensitive to one erroneous minimum than P_0 while retaining the lower-tail behavior of the horizontal beach buffer. It is not mathematically equivalent to the conventional vertical $R_{2\%}$ statistic: P_2 was obtained from frame-wise horizontal RBW, whereas $R_{2\%}$ is a vertical elevation exceeded by 2% of individual wave-runup maxima. For traceability, the original timestack and final-trajectory overlay, row-level trajectory table containing the original automatic and final reviewed positions, correction fields, pixel and map coordinates, Otsu thresholds, saved detector settings, operator and session metadata, and final status, together with trajectory-summary, chunk, session-specific trajectory-comparison, percentile-sensitivity, audit-summary, and correction-region records, were retained. Binary candidate masks and intermediate feature images were used internally but were not archived; the detection-step export option was disabled in all saved settings. During pre-analysis candidate screening, observation periods were excluded when the active swash zone was not visible, the orthorectified domain did not contain the full landward excursion, or the runup front remained ambiguous after inspection and correction.

For the 514–600 finite Analyst 1 positions retained per trajectory, unavailable positions were omitted without temporal interpolation. Under the linear percentile definition, P_2 fell between adjacent order statistics spanning the 11th–13th ordered finite positions across this range of valid sample sizes. Percentile sensitivity was evaluated by recalculating the Analyst 1 RBW summaries at P_0, P_1, P_5, and P_{10} and comparing them with the primary P_2 values; downstream CCTV–Stockdon agreement metrics were also recomputed. P_2 was retained as the prespecified operational compromise between a single-frame minimum and higher lower-tail percentiles; it was not selected post hoc to maximize agreement with the Stockdon-derived values.

The same 120 source timestacks, corresponding to 60 observation periods and two fixed transects, were interpreted separately by Analyst 1 and Analyst 2 using the same source images, preprocessing workflow, runup-front definition, and quality-control criteria. For each timestack, the automatic trajectory could be retained or manually corrected based solely on the analyst's visual judgment; neither analyst was required to reproduce the other analyst's interventions. A separate set of 120 trajectories was therefore generated by each analyst. The complete Analyst 1 series was used for the primary analysis, whereas the Analyst 2 series was used only to quantify inter-analyst reproducibility. Percentile summaries were calculated from finite final RBW positions after the non-negative convention had been applied; unavailable positions were omitted. Each Analyst 1 trajectory retained 514–600 finite positions. Intervention statistics and inter-analyst agreement are reported in Section 3.2.

Inter-analyst reproducibility was assessed by pairing the two final trajectory summaries for each of the 120 matched source timestacks. Analyst 1 was retained for the primary CCTV–Stockdon comparisons, whereas Analyst 2 was used only for the reproducibility assessment. The paired comparison is shown in Figure 7. Agreement was summarized using bias, MAE, RMSE, Pearson r, and Bland–Altman 95% limits of agreement.

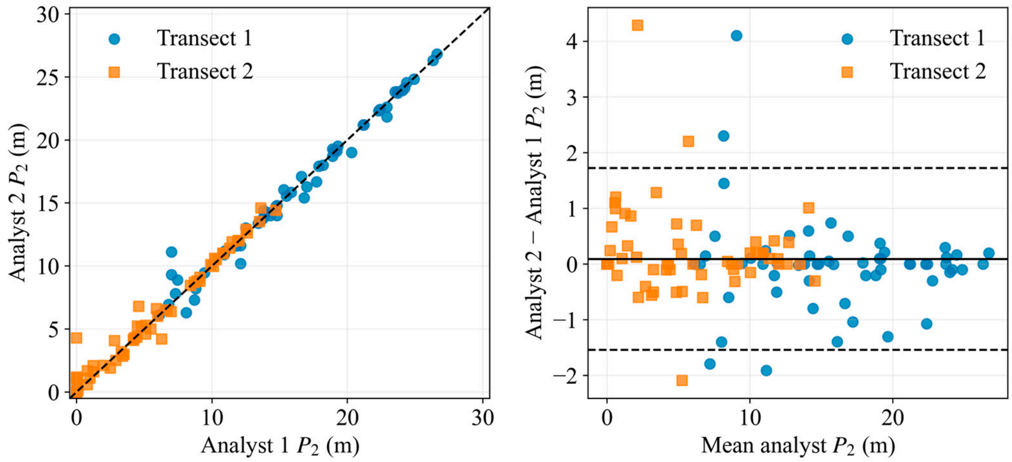

Figure 7. Inter-analyst agreement for 60 CCTV observation periods (120 paired trajectory interpretations): 1:1 comparison and difference-versus-mean diagnostic with mean difference and 95% limits of agreement.

2.3. Stockdon-Derived RBW Estimation

2.3.1. Beach-Morphology and Water-Level Inputs

Stockdon-derived RBW was estimated separately for Transects 1 and 2 using wave conditions, surveyed beach-profile morphology, and observation-time water levels. The study-period candidate pool contained 11 survey dates from 23 August 2023 to 11 March 2026 (Table 1). Each survey supplied transect-specific beach width and foreshore slope. For the primary CCTV–Stockdon comparison, the temporally nearest candidate survey was assigned to each CCTV observation period; seven of the 11 dates were selected as nearest for at least one of the 60 periods. The same nearest-survey rule was applied to the Q_{95} and survey-matched cohorts. The survey-matched cohort had relatively small offsets, whereas the Q_{95} cohort included energetic periods for which the nearest survey could be substantially more distant. All 11 survey states, including dates that were not selected as nearest in the primary comparison, were retained for the paired morphology-input sensitivity analysis described in Section Paired Morphology-Input Timing Sensitivity Analysis. A local cross-shore coordinate was defined as positive seaward, with the origin at the intersection of each transect and the coastal baseline. Surveyed beach width was defined as the horizontal distance from the coastal baseline to the reference shoreline:

$$W = x_{\mathrm{SL}} - x_B \tag{9}$$

where x_{SL} is the reference-shoreline position and $x_B = 0$ is the coastal-baseline position. Consequently, W represents the horizontal beach width between the coastal baseline and the reference shoreline along each transect. The foreshore slope used in the Stockdon parameterization was expressed as a dimensionless gradient:

$$m_f = \tan\beta_f \tag{10}$$

The Hupo tide gauge is located approximately 39.3 km in straight-line distance from the midpoint of Namho Beach. The nearest one-minute water-level observation was matched to the central timestamp of each 10 min CCTV observation period, with a maximum absolute time difference of 29.5 s. The supplied gauge series was converted to the IMSL-referenced profile datum as $\eta = (z_g - 21.34)/100$ m, where z_g denotes the gauge reading in centimeters. The 21.34 cm constant represents the offset between the Hupo gauge datum and the IMSL-referenced beach-profile datum. The Hupo record was the nearest available regional water-level record, but local wave setup, harbor effects, and all site-specific non-tidal residuals may not have been represented. It was therefore used as a regional proxy rather than as local in situ validation. Water levels and profile elevations were referenced to a common vertical datum.

Table 1. Eleven study-period beach-profile surveys available as Stockdon morphology inputs. Seven survey dates were selected as nearest for at least one observation period in the primary comparison; all 11 survey states were used in the paired morphology-input sensitivity analysis.

Survey Date	Transect 1		Transect 2	
	W (m)	**β_f (°)**	**W (m)**	**β_f (°)**
23 August 2023	23.40	7.6	15.90	8.9
13 December 2023	30.90	5.2	18.60	4.8
28 February 2024	29.54	5.5	19.83	5.1
22 April 2024	20.64	6.1	14.29	5.7
8 August 2024	15.86	6.1	13.98	5.5
1 November 2024	17.37	7.3	11.76	4.0
19 February 2025	33.03	3.9	22.26	4.4
17 April 2025	24.57	6.5	17.65	5.0
13 August 2025	21.78	3.8	13.44	5.9
30 October 2025	22.68	5.4	14.71	4.4
11 March 2026	29.70	5.3	18.10	3.9

2.3.2. Stockdon Runup Calculation and Conversion to RBW

The 2% exceedance vertical runup elevation $R_{2\%}$ was calculated using the empirical parameterization of Stockdon et al. [3]. The deep-water wavelength L_0 was computed from the peak wave period T_p as

$$L_0 = \frac{gT_p^2}{2\pi} \tag{11}$$

The ADCP H_{m0} at approximately 24 m depth was transformed to deep-water H_0 before the primary Stockdon calculation using the reverse-shoaling procedure in Section 2.3.3.

$$H_0 = H_{24}\sqrt{\frac{C_{g,24}}{C_{g,0}}} \tag{12}$$

The deep-water surf-similarity parameter was calculated as

$$\xi_0 = \frac{m_f}{\sqrt{H_0/L_0}} \tag{13}$$

where m_f is the dimensionless foreshore slope defined in Section 2.3.1. For intermediate to reflective beach conditions, the Stockdon et al. [3] parameterization was applied as

$$R_{2\%} = 1.1\left[0.35m_f(H_0L_0)^{1/2} + \frac{\left[H_0L_0\left(0.563m_f^2 + 0.004\right)\right]^{1/2}}{2}\right] \tag{14}$$

For highly dissipative conditions, defined by $\xi_0 < 0.3$, the slope-independent expression proposed by Stockdon et al. [3] is

$$R_{2\%} = 0.043(H_0L_0)^{1/2} \tag{15}$$

In the present analysis, the calculated surf-similarity parameter ranged from 0.37 to 1.25 at Transect 1 and from 0.38 to 1.09 at Transect 2. No retained observation-period–transect record satisfied the highly dissipative criterion. The general Stockdon expression in Equation (14) was therefore applied to all records. Sediment grain size and incident wave direction are not explicit inputs to the Stockdon parameterization; they were retained for site and wave-condition characterization but were not used in the runup calculation. The normal-incidence transformation described below was retained for the primary calculation; oblique incidence was examined only in an auxiliary sensitivity analysis, and directional spreading was not quantified. The observation-time runup level was calculated by adding the observed water level to the Stockdon runup elevation:

$$Z_{2\%} = \eta(t) + R_{2\%} \tag{16}$$

where the observed water level was referenced to the same vertical datum as the terrestrial beach profiles. The resulting runup level therefore included the astronomical tide and the non-tidal residual represented in the Hupo record. Assuming that the foreshore between the reference shoreline and predicted runup location could be represented locally by a planar slope, the observation-time runup level was converted to horizontal landward excursion as

$$X_{2\%} = \frac{Z_{2\%} - z_{\mathrm{SL}}}{m_f} \tag{17}$$

where z_{SL} is the elevation of the reference shoreline in the adopted vertical datum. In the present analysis, the reference shoreline was defined at $z_{SL} = 0$, and Equation (17) therefore reduces to

$$X_{2\%} = \frac{\eta(t) + R_{2\%}}{m_f} \tag{18}$$

The raw Stockdon-derived RBW was then calculated by subtracting the predicted horizontal landward excursion from the surveyed beach width:

$$RBW_{\mathrm{Stockdon,raw}} = W - X_{2\%}, \tag{19}$$

where W is the surveyed horizontal distance from the coastal baseline to the reference shoreline and $X_{2\%}$ is the estimated landward horizontal excursion from that shoreline. For consistency with the CCTV-derived RBW calculation, a non-negative RBW convention was applied. When the predicted Stockdon runup position reached or exceeded the coastal baseline, the corresponding RBW was set to 0 m:

$$RBW_{\mathrm{Stockdon}} = \max(RBW_{\mathrm{Stockdon,raw}}, 0). \tag{20}$$

Smaller RBW_{Stockdon} values indicate a greater landward extent of the predicted runup and a narrower remaining beach buffer. A value of 0 m indicates that the predicted runup position reached or exceeded the coastal baseline under the non-negative RBW convention. The same coastal baseline, transect coordinate system, horizontal coordinate reference system, and beach-width definition were used for both the CCTV-derived and Stockdon-derived RBW calculations.

2.3.3. Reverse-Shoaling Transformation and Wave-Input Sensitivity Analysis

Because the ADCP was deployed at approximately 24 m depth, each measured H_{24} was transformed to a deep-water-equivalent wave height H_0 using linear wave theory. For each peak period T_p, the angular frequency was defined as $\omega = 2\pi/T_p$, and the wavenumber k was obtained by solving

$$\omega^2 = g\,k\,\tanh(k\,h) \tag{21}$$

where g is gravitational acceleration and h is water depth. The finite-depth group velocity was evaluated as

$$C_g = n\frac{\omega}{k}, \qquad n = \left(\frac{1}{2}\right)\left[1 + \frac{2\,k\,h}{\sinh(2\,k\,h)}\right] \tag{22}$$

where n is the group-velocity coefficient. The deep-water group velocity was calculated as

$$C_{g,0} = g\frac{T_p}{4\pi} \tag{23}$$

Equation (22) was evaluated at $h = 24$ m to obtain $C_{g,24}$. Under the assumptions of normal incidence, linear propagation, and negligible dissipation, H_0 was obtained from conservation of wave-energy flux using Equation (12), with $C_{g,0}$ from Equation (23). The primary Stockdon $R_{2\%}$ and RBW values were calculated using this normal-incidence H_0.

An auxiliary wave-input sensitivity analysis was conducted using the 1224 hourly records in the supplied energetic-condition wave table. The assumed ADCP depth was varied from 20 to 28 m in 2 m increments. Peak wave direction, θ_p, was taken from the processed ADCP field Peak Direction (DirTp) and was treated as a waves-from compass azimuth referenced to north and increasing clockwise (0° = north; 90° = east). The supplied directional values were used without additional angular rotation. The seaward-normal azimuth of each transect was calculated clockwise from the northing axis of the projected survey coordinates. Oblique-incidence sensitivity was evaluated by defining the local incidence angle as the minimum absolute circular difference between θ_p and the corresponding seaward-normal azimuth (84.53° for Transect 1 and 72.44° for Transect 2). Deep-water angle and wave height were then estimated using Snell refraction and conservation of cross-shore wave-energy flux. Solutions without a valid inverse-Snell angle or with a deep-water incidence angle greater than 75° were not used to summarize stable oblique results. Because only a single peak direction, rather than a frequency–direction spectrum, was available, directional spreading was not quantified. The oblique calculation also assumed parallel contours, linear refraction, and negligible dissipation and was therefore retained as a sensitivity analysis rather than as the primary transformation.

2.4. CCTV–Stockdon Comparison and Statistical Evaluation

CCTV-derived and Stockdon-derived RBW estimates were paired by CCTV observation time and transect. Each comparison therefore represented one observation-period–transect record for which both a CCTV-derived lower-tail horizontal RBW and a Stockdon-derived horizontal RBW were available. For paired record i, the CCTV–Stockdon difference was defined as

$$e_i = RBW_{CCTV,i} - RBW_{Stockdon,i} \tag{24}$$

This sign convention was adopted throughout. A positive difference indicates that the CCTV-derived remaining buffer was wider than the Stockdon-derived estimate, whereas a negative value indicates that the CCTV runup front was farther landward. The complete dataset contained 60 observation periods and 120 observation-period–transect records. Dataset-specific summaries contained 35 Q_{95} observation periods (70 observation-period–transect records) and 25 survey-matched observation periods (50 records), without overlap. Agreement was quantified using bias, mean absolute error (MAE), RMSE, NSE, and Pearson r. Mean bias was calculated as

$$\text{Bias} = \frac{1}{N}\sum_{i=1}^{N} e_i \tag{25}$$

where N is the number of paired observation-period–transect comparisons. The mean absolute error was calculated as

$$\text{MAE} = \frac{1}{N}\sum_{i=1}^{N}|e_i| \tag{26}$$

The root-mean-square error was calculated as

$$\text{RMSE} = \sqrt{\frac{1}{N}\sum_{i=1}^{N}e_i^2} \tag{27}$$

The Nash–Sutcliffe efficiency (NSE) [22] was calculated as

$$NSE = 1 - \frac{\sum_{i=1}^{N}\left(RBW_{\text{CCTV},i} - RBW_{\text{Stockdon},i}\right)^2}{\sum_{i=1}^{N}\left(RBW_{\text{CCTV},i} - \overline{RBW}_{CCTV}\right)^2} \tag{28}$$

where $\overline{RBW}_{CCTV}$ is the mean CCTV-derived RBW. NSE was used to evaluate the predictive agreement of Stockdon-derived RBW relative to CCTV-derived RBW. Negative NSE values indicate that the Stockdon-derived estimates performed worse than using the mean CCTV-derived RBW as a reference prediction. The Pearson correlation coefficient was used to quantify the linear association between the two RBW estimates:

$$r = \frac{\sum_{i=1}^{N}\left(RBW_{\text{Stockdon},i} - R\bar{B}W_{\text{Stockdon}}\right)\left(RBW_{\text{CCTV},i} - R\bar{B}W_{\text{CCTV}}\right)}{\sqrt{\sum_{i=1}^{N}\left(RBW_{\text{Stockdon},i} - R\bar{B}W_{\text{Stockdon}}\right)^2}\sqrt{\sum_{i=1}^{N}\left(RBW_{\text{CCTV},i} - R\bar{B}W_{\text{CCTV}}\right)^2}} \tag{29}$$

Statistics were calculated separately for the Q_{95} and survey-matched cohorts and for Transects 1 and 2. The between-dataset comparison was used to describe dataset-specific agreement, not to isolate the effect of morphology timing, because the hydrodynamic composition differed between the datasets. CCTV-derived P_2 RBW and Stockdon-derived RBW were obtained by different observational and empirical procedures. Their comparison was therefore interpreted as agreement between two operational estimates of horizontal wave reach, not as validation against ground truth or as evidence of mathematical equivalence.

Dependence was handled explicitly. For the Q_{95} cohort, a new wave-episode cluster was initiated when the interval between consecutive observation periods exceeded 24 h, yielding 30 clusters; cluster counts obtained using 12- and 48 h separation rules were reported as sensitivity checks. The survey-matched cohort was clustered by the five morphology-survey epochs. Two-sided 95% confidence intervals were calculated using a nonparametric percentile cluster bootstrap based on the 2.5th and 97.5th percentiles of 2000 replicates. In each replicate, the original number of clusters was sampled with replacement, and all observation periods within each selected cluster were retained. Identical cluster-draw sequences were applied to the two transect-specific analyses so that paired observation periods were selected synchronously. Calculations were implemented in Python 3.12.13 (Python Software Foundation, Beaverton, OR, USA) using NumPy 2.3.5 (NumPy Developers) and pandas 3.0.1 (The Pandas development team), with NumPy's default_rng initialized using a fixed seed of 20260720. Because only five survey-epoch clusters were available, the survey-matched confidence intervals were interpreted cautiously.

The 120 trajectory records comprised paired transects from 60 observation periods and were not treated as independent observations. Consecutive Q_{95} observation periods could also belong to the same wave episode. The cluster rules described above were therefore used for inference.

Paired Morphology-Input Timing Sensitivity Analysis

A controlled input-sensitivity analysis was used to distinguish morphology timing from differences between the Q_{95} and survey-matched cohorts. The candidate morphology pool comprised 11 surveys dated 23 August 2023, 13 December 2023, 28 February 2024, 22 April 2024, 8 August 2024, 1 November 2024, 19 February 2025, 17 April 2025, 13 August 2025, 30 October 2025, and 11 March 2026. An observation period was eligible when its closest survey date was within 5 calendar days of the CCTV observation date. Acquisition hours were retained for the five surveys used to construct the survey-matched cohort and were used to select the common hourly observations described in Section 2.2.1. Across the full pool of 11 morphology surveys; however, survey dates were archived consistently whereas sub-daily acquisition times were not. Eligibility and the close and distant classification were therefore evaluated using calendar-day offsets. The criterion yielded 27 observation periods and 54 paired observation-period–transect records. The corresponding wave-reference times, matched survey times, calendar-day offsets, and distant-survey counts are provided in Appendix A (Table A3). For each record, CCTV-derived P_2 RBW, reverse-shoaled wave height, peak period, observation-time water level, transect, and coastal baseline were held fixed, and Stockdon-derived RBW was recalculated using the beach width and foreshore slope from each of the 11 morphology surveys.

For each eligible record, the close discrepancy was the absolute CCTV–Stockdon difference obtained using the nearest morphology. The distant discrepancy was the record-specific median of the absolute differences obtained using survey states separated from the CCTV observation date by at least 30 calendar days. Every eligible record had one close scenario and 10 distant scenarios. A paired close-minus-distant contrast was calculated for each transect record, and the two transect-specific contrasts were averaged within each observation period. Because the 27 eligible periods were nested within only five close-survey epochs, the observation-period contrasts were grouped by epoch and summarized descriptively as a finite-scenario input-sensitivity result rather than as a population-level causal effect of survey age. Separately, across all 60 observation periods, Spearman rank correlation between nearest-survey calendar-day offset and observation-period-mean absolute CCTV–Stockdon difference was reported descriptively. For additional summaries, nearest-survey offsets were grouped into right-closed bins of $[0, 1]$, $(1, 7]$, $(7, 14]$, $(14, 30]$, and $(30, 60]$ days. No causal comparisons among bins were inferred.

3. Results

3.1. Temporal Variability of Beach Morphology

Temporal variability in beach morphology was identified from 41 terrestrial beach-profile surveys at each transect (Figure 8). Mean beach width was 27.19 m at Transect 1 (SD = 5.93 m; CV = 21.80%) and 20.65 m at Transect 2 (SD = 5.08 m; CV = 24.62%) (Table 2). Transect 2 was therefore narrower on average, while similar relative variability was observed at both transects. Foreshore slope also varied through time and affected the conversion of vertical $R_{2\%}$ to horizontal excursion. The surveyed morphology was non-stationary, providing the basis for the paired morphology-input sensitivity analysis.

Table 2. Summary statistics of long-term terrestrial beach width at Transects 1 and 2.

	n	**Mean *W* (m)**	**SD *W* (m)**	**CV (%)**
Transect 1	41	27.19	5.93	21.80
Transect 2	41	20.65	5.08	24.62

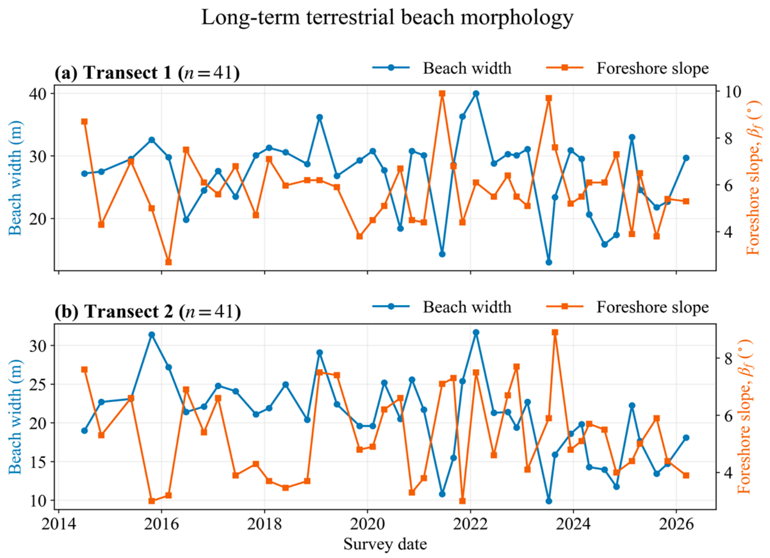

Figure 8. Terrestrial morphology from 41 surveys at each transect: beach width and foreshore slope at (**a**) Transect 1 and (**b**) Transect 2.

3.2. Comparison Between CCTV-Derived and Stockdon-Derived RBW

Primary agreement statistics were calculated from the complete Analyst 1 series (60 observation periods; 120 trajectory records) using reverse-shoaled H_0. Bias was defined as CCTV-derived P_2 RBW minus Stockdon-derived RBW. For Q_{95} Transect 1 ($n = 35$), bias was +2.66 m, MAE was 4.27 m, RMSE was 5.55 m, r was 0.66, and NSE was 0.18. For Q_{95} Transect 2 ($n = 35$), bias was +0.23 m, MAE was 3.50 m, RMSE was 4.53 m, r was 0.24, and NSE was −0.44. Poor predictive agreement at Transect 2 was indicated by the negative NSE and weak correlation despite the small mean bias.

For the survey-matched cohort, Transect 1 ($n = 25$) had a bias of −2.50 m, MAE of 2.80 m, RMSE of 3.53 m, r of 0.89, and NSE of 0.58. Transect 2 ($n = 25$) had a bias of −1.76 m, MAE of 2.10 m, RMSE of 2.62 m, r of 0.90, and NSE of 0.65. Because the hydrodynamic composition differed from that of the Q_{95} cohort, the stronger survey-matched statistics did not by themselves demonstrate an effect of morphology timing.

Manual intervention was quantified for both separate interpretations. Analyst 1 corrected 78 of 120 trajectories (65.0%) from 49 of 60 observation periods (81.7%), affecting 28,899 of 72,000 frame records (40.1%); the median of the trajectory-specific median absolute correction magnitudes was 1.38 m. Analyst 2 corrected 75 of 120 trajectories (62.5%) from 49 of 60 periods (81.7%), affecting 18,624 of 72,000 frame records (25.9%); the corresponding median absolute magnitude was 1.13 m. For P_2 RBW, the Analyst 2-minus-Analyst 1 bias was +0.09 m, MAE was 0.45 m, RMSE was 0.83 m, and $r = 0.994$. The Bland–Altman 95% limits of agreement were −1.54 to +1.72 m; the median and P_{95} absolute differences were 0.20 and 1.80 m, respectively (Figure 7).

Percentile sensitivity was non-negligible. Relative to the Analyst 1 P_2 values, the median absolute differences were 0.50 m for P_1, 1.00 m for P_5, 1.27 m for P_0, and 2.00 m for P_{10}; the corresponding P_{95} differences were 1.30, 3.29, 4.19, and 5.00 m. Downstream agreement statistics also changed with the selected percentile, supporting interpretation of P_2 as a prespecified operational statistic rather than a percentile-insensitive or agreement-optimized quantity. The four primary CCTV–Stockdon comparisons are shown in Figure 9.

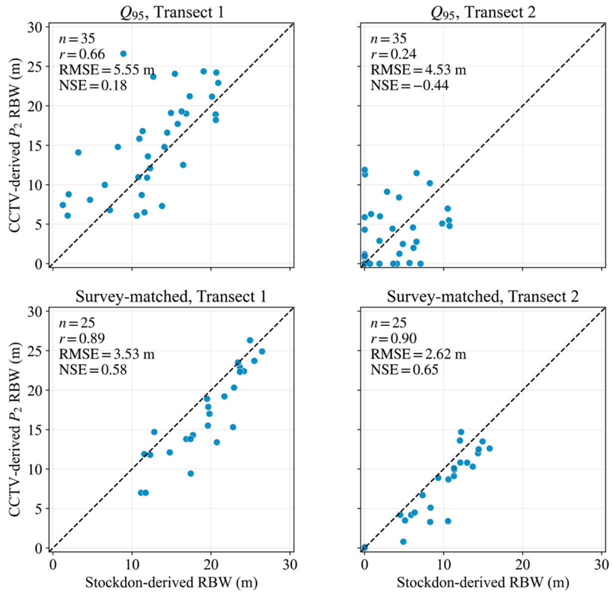

Figure 9. CCTV-derived P_2 RBW versus Stockdon-derived RBW calculated using reverse-shoaled deep-water-equivalent H_0 with common axes and a 1:1 line for Q_{95} and survey-matched cohorts at both transects.

The corresponding sample sizes, bias, MAE, RMSE, NSE, Pearson r, and cluster-bootstrap confidence intervals are reported in Table 3.

Table 3. Agreement statistics between CCTV-derived P_2 RBW and Stockdon-derived RBW calculated using reverse-shoaled deep-water-equivalent H_0. Values in brackets are two-sided 95% percentile cluster-bootstrap confidence intervals (2000 replicates).

	Transect 1		**Transect 2**	
	Q_{95} Cohort	**Survey-Matched Cohort**	**Q_{95} Cohort**	**Survey-Matched Cohort**
n	35	25	35	25
NSE	0.18 [−0.30, 0.55]	0.58 [−0.14, 0.80]	−0.44 [−1.17, 0.07]	0.65 [0.01, 0.78]
RMSE (m)	5.55 [3.87, 7.23]	3.53 [2.03, 4.78]	4.53 [3.39, 5.65]	2.62 [2.10, 3.10]
MAE (m)	4.27 [3.14, 5.51]	2.80 [1.75, 4.05]	3.50 [2.55, 4.57]	2.10 [1.81, 2.35]
Bias (m)	+2.66 [0.88, 4.36]	−2.50 [−3.90, −1.14]	+0.23 [−1.33, 1.81]	−1.76 [−2.34, −0.83]
Pearson r	0.66 [0.43, 0.82]	0.89 [0.77, 0.95]	0.24 [−0.11, 0.54]	0.90 [0.72, 0.97]

For the 27 observation periods whose nearest survey was within 5 days, 54 observation-period–transect records were recalculated using all 11 study-period morphology surveys. Each record contributed one closest-survey scenario and 10 distant-survey scenarios, all at least 30 calendar days from the observation. The mean absolute CCTV–Stockdon difference obtained using the closest morphology was 2.49 m, whereas the mean of the record-specific medians across the 10 distant scenarios was 4.43 m, yielding a descriptive paired close-minus-distant contrast of −1.94 m. After the two transects were averaged within each observation period, the contrast was negative in 21 of 27 periods and in four of the five close-survey epochs; mean contrasts were −2.90 m at Transect 1 and −0.98 m at Transect 2. Across all 60 observation periods, the descriptive association between observation-period-mean absolute difference and nearest-survey offset was weak ($\rho = 0.381$), with a weak association at Transect 1 ($\rho = 0.346$) and a negligible association at Transect 2 ($\rho = 0.053$). Thus, temporally close morphology was associated with a smaller discrepancy for this selected finite set of inputs; a general causal effect of survey age was not inferred.

Morphology timing was defined as the absolute calendar-day difference between each hourly wave-reference date and its assigned survey date. Right-closed bins of $[0, 1]$,

$(1, 7]$, $(7, 14]$, $(14, 30]$, and $(30, 60]$ days contained 28, 26, 16, 24, and 26 observation-period–transect records, respectively.

Agreement was heterogeneous: the Q_{95} Transect 1 result showed moderate association with appreciable error, Q_{95} Transect 2 showed poor agreement, and the survey-matched cohort showed stronger agreement. The paired sensitivity analysis showed that temporal representativeness of morphology was an important input uncertainty, but it did not explain all CCTV–Stockdon differences. The observation-period and survey-epoch contrasts are shown in Figure 10.

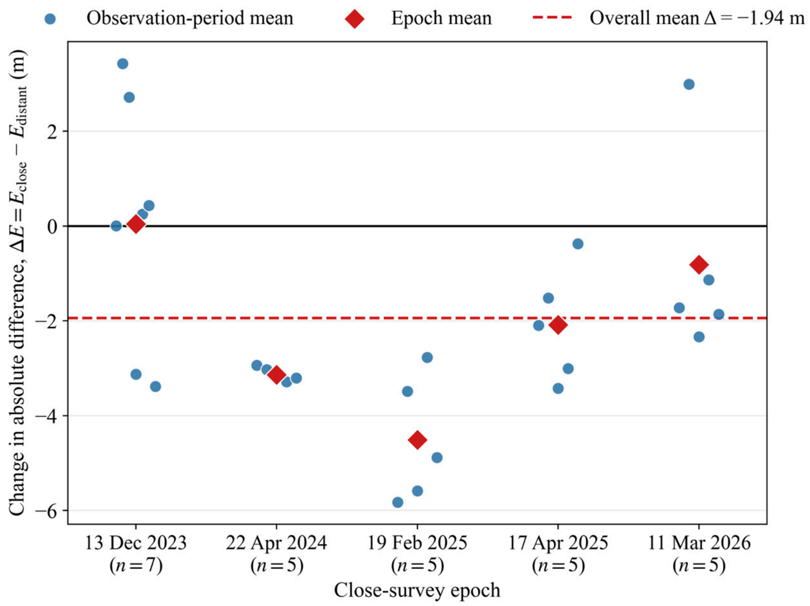

Figure 10. Observation-period-level paired morphology-input contrasts for the 27 eligible periods, grouped by the five close-survey epochs. For each period, the two transect-specific contrasts were averaged after CCTV-derived RBW, wave conditions, water level, transect, and coastal baseline had been held fixed. The contrast is the absolute CCTV–Stockdon difference obtained with the nearest morphology (within 5 calendar days) minus the record-specific median obtained from the 10 distant morphology states (at least 30 calendar days). Negative values indicate a smaller empirical-comparison discrepancy with the nearest morphology. Points show observation periods, diamonds show epoch means, and the dashed line shows the overall mean (−1.94 m). The figure describes sensitivity to the finite set of tested morphology inputs and is not an accuracy validation or a causal test of elapsed time.

3.3. Reverse-Shoaling and Wave-Input Sensitivity Analysis

Across the 60 observation periods, the median H_0/H_{24} ratio was 1.078, and only 6 of 60 periods satisfied the conventional deep-water criterion $h/L \geq 0.5$ at the ADCP. Reverse shoaling increased Stockdon $R_{2\%}$ by a median of 3.83% (mean, 3.27%) and decreased raw Stockdon-derived RBW by 0.50 m on average. After application of the non-negative RBW convention, the mean decrease was 0.41 m (range, 0–0.98 m). The finite-depth correction was therefore smaller than the observed CCTV–Stockdon RMSE. These primary values assumed normal incidence and did not include dissipation or directional spreading.

In the auxiliary 1224-record sensitivity analysis, the median normal-incidence H_0/H_{24} ratio at 24 m was 1.083, and the corresponding median Stockdon $R_{2\%}$ increase was 4.07%. Across assumed depths of 20–28 m, median H_0/H_{ADCP} ranged from 1.075 to 1.089 and the median $R_{2\%}$ increase ranged from 3.67% to 4.36%. Median local incidence angles were 11.3° and 12.5° at Transects 1 and 2, respectively. Among stable oblique solutions, median H_0/H_{24} was 1.089 at Transect 1 ($n = 1217$) and 1.088 at Transect 2 ($n = 1215$), corresponding to median $R_{2\%}$ increases of 4.35% and 4.30%. These values were close to the normal-incidence sensitivity, but they were not adopted in the primary calculation because the simplified analysis did not represent complex bathymetry, dissipation, or directional spreading.

4. Discussion

4.1. CCTV-Derived RBW as a Time-Resolved Observational Metric

Orthorectified coastal CCTV imagery was used to quantify RBW in map coordinates. After the oblique imagery had been transformed to plan view, runup-front positions were extracted along fixed transects and expressed as the horizontal distance remaining between the landward limit of visually identifiable wave-induced whitewater and the coastal baseline. Each 10 min observation period yielded a 600-row trajectory series, and lower-tail P_2 RBW was calculated from its finite reviewed positions. The method therefore supplied time-resolved observations of horizontal beach-buffer reduction between intermittent terrestrial surveys. However, the metric was conditional on image visibility, analyst interpretation, and the planar orthorectification.

CCTV-derived RBW was obtained directly from time-resolved runup-front positions, whereas Stockdon-derived RBW was obtained by converting an empirical vertical $R_{2\%}$ elevation to horizontal excursion using assigned beach morphology and water level. Because the two metrics have different statistical and physical definitions, their comparison was interpreted as agreement between operational estimates of horizontal wave reach. Stockdon-derived RBW was not treated as ground truth.

4.2. Interpretation of the CCTV–Stockdon Comparison

Dataset- and transect-dependent agreement was obtained. For the Q_{95} cohort, a moderate association was observed at Transect 1 ($r = 0.66$), but the RMSE remained 5.55 m and NSE was 0.18; poor predictive agreement was obtained at Transect 2 ($r = 0.24$; NSE = -0.44; RMSE = 4.53 m). Stronger agreement was obtained for the survey-matched cohort at both transects (r = 0.89–0.90; NSE = 0.58–0.65; RMSE = 2.62–3.53 m). The latter comparison described a different hydrodynamic sample and did not independently identify a morphology-timing effect.

4.3. Influence of Morphology Timing and Local Beach Geometry

The sensitivity of Stockdon-derived RBW to morphology input was evaluated while the CCTV observation, wave conditions, water level, and transect were held fixed. For the selected finite set of tested inputs, morphology acquired within 5 days was associated with an absolute CCTV–Stockdon difference 1.94 m smaller than the record-specific median obtained from 10 survey states at least 30 days distant. The observation-period contrast was negative in 21 of 27 periods and in four of five close-survey epochs, but the nearest-offset association was weak overall and negligible at Transect 2. Temporal representativeness of morphology was therefore treated as a conditional input uncertainty, not as a universal linear control or a causal effect of survey age.

Temporal mismatch affects the beach width and foreshore slope assigned to an observation period and therefore affects both the initial horizontal buffer and the conversion of vertical $R_{2\%}$ to horizontal excursion. Its influence depends on the morphology state assigned, not on elapsed time alone.

The paired contrast and nearest-offset results are summarized in Figure 10 and Table 4. Considerable overlap remained among error distributions; image interpretation, camera geometry, regional water-level representation, wave transformation, and the assumptions of the Stockdon parameterization therefore remained plausible contributors.

Table 4. Analyst 1 absolute CCTV–Stockdon RBW differences grouped by calendar-day offset between each CCTV observation date and its nearest assigned morphology survey (120 observation-period–transect records).

Calendar-Day Offset (Days)	n	Mean Absolute RBW Difference (m)	Median Absolute RBW Difference (m)
$[0, 1]$	28	2.86	2.17
$(1, 7]$	26	2.09	1.69
$(7, 14]$	16	4.65	3.52
$(14, 30]$	24	3.04	2.95
$(30, 60]$	26	4.33	3.90

The transect-dependent results may partly reflect local beach geometry. Transect 2 was narrower than Transect 1, so a similar absolute error in runup-front position, surveyed beach width, or morphology assignment would represent a larger fraction of the available beach buffer. This interpretation remains qualitative because the two-transect design did not permit the effects of local geometry to be isolated.

Although stronger survey-matched statistics were obtained at Transect 2, the paired analysis and near-zero Transect 2 offset correlation did not support attribution of the between-dataset difference to morphology timing alone.

4.4. Practical Applicability for Coastal Monitoring

CCTV-derived RBW can complement intermittent terrestrial beach-profile surveys by providing repeated observations of runup-front motion during energetic conditions. Once the camera geometry, coastal baseline, and transects have been established, horizontal beach-buffer reduction can be estimated from time-resolved imagery between survey epochs.

The approach should not be used as a replacement for terrestrial surveys. Periodic surveys remain required to update beach width, foreshore slope, and vertical morphology and to supply morphology inputs when an empirical runup parameterization is applied. CCTV observations and field surveys should therefore be interpreted as complementary components of the monitoring system.

4.5. Limitations and Future Improvements

Several limitations should be considered. First, CCTV-derived RBW depended on visibility and optical detectability of the runup front. Low contrast, shadows, sun glare, residual foam, wet-sand reflectance, passing objects, and partial obstruction could affect automated detection. Manual inspection and correction were therefore required for 65.0% of Analyst 1 trajectories. Although the inter-analyst RMSE was 0.83 m, the P_{95} absolute difference was 1.80 m, indicating that interpretation uncertainty was small on average but non-negligible for individual trajectories. More robust automated segmentation should be evaluated against independently interpreted trajectories in future applications.

Second, geometric uncertainty was material. The withheld-checkpoint 2D RMSE was 3.29 m, compared with a 1.45 m internal calibration RMSE. The checkpoints were independent of homography fitting but shared the survey reference framework. Projection of all five residual vectors onto the transect directions yielded cross-shore RMSE values of 0.59 m at Transect 1 and 0.21 m at Transect 2. However, sparse local checkpoints, extrapolation of the transect origins beyond the calibration hull, and the horizontal-plane assumption limited these transect-resolved values to empirical checks rather than a complete propagated accuracy model. The geometric error scale was therefore reported alongside, but not subtracted from, the 2.62–5.55 m CCTV–Stockdon comparison RMSE.

Third, reverse shoaling addressed the finite-depth inconsistency in the wave-height input, but the Stockdon-derived RBW calculation still assumed linear, normally incident, nondissipative transformation, a locally planar foreshore, and a regional tide-gauge proxy. Oblique incidence was evaluated only through a simplified peak-direction sensitivity analysis and was not used in the primary transformation. Directional spreading could not be quantified because a frequency–direction spectrum was unavailable. These assumptions further support use of Stockdon-derived RBW as an empirical comparator rather than as ground truth.

Fourth, the UAV orthomosaic was not used as independent validation of instantaneous runup position because a spatial mosaic acquired over a finite period does not preserve frame-scale swash-front motion. UAV and RTK data were used only to support definition of the coastal baseline, interpretation of beach configuration, and assessment of the orthorectified imagery.

Finally, the analysis was limited to two transects at one sandy beach. The transferability of the method to other beach slopes, sediment characteristics, tidal ranges, camera geometries, and wave climates was therefore not established.

Overall, time-resolved horizontal beach-buffer observations were obtained from CCTV imagery, but agreement with Stockdon-derived RBW was heterogeneous. In the selected finite input-sensitivity set, temporally representative morphology was associated with lower empirical-comparison error under the tested conditions. Interpretation remained conditional on the withheld-checkpoint assessment, analyst reproducibility, regional water-level representation, wave-transformation assumptions, and the horizontal mapping-plane approximation.

5. Conclusions

CCTV-derived RBW was evaluated for 60 selected 10 min observation periods at Namho Beach, and the sensitivity of Stockdon-derived RBW to morphology timing was evaluated separately. Primary results were obtained from the complete Analyst 1 series, and inter-analyst reproducibility was quantified through second-analyst reinterpretation of the same 120 trajectory records.

CCTV-derived P_2 RBW is a horizontal lower-tail statistic, whereas Stockdon $R_{2\%}$ is an empirical vertical exceedance elevation converted to horizontal distance. The metrics are not statistically equivalent, and Stockdon-derived RBW was used as an empirical comparator rather than as ground truth.

For the Q_{95} cohort, association was moderate at Transect 1 ($r = 0.66$), but RMSE remained 5.55 m and NSE was 0.18; agreement was poor at Transect 2 ($r = 0.24$; RMSE = 4.53 m; NSE = -0.44). Agreement was stronger in the survey-matched cohort (r = 0.89–0.90; RMSE = 2.62–3.53 m; NSE = 0.58–0.65). In the paired morphology-input sensitivity analysis, the absolute difference with morphology acquired within 5 days was descriptively 1.94 m smaller than the record-specific median obtained from 10 survey states at least 30 days distant. The contrast was negative in 21 of 27 periods and four of five survey epochs. Because the nearest-offset association was weak and transect-dependent, a general causal effect of morphology timing was not inferred, and morphology timing did not alone explain the CCTV–Stockdon differences.

The withheld-checkpoint 2D RMSE was 3.29 m. When all five checkpoint residual vectors were projected onto the fixed transect directions, directional cross-shore RMSE values of 0.59 m at Transect 1 and 0.21 m at Transect 2 were obtained; these were empirical directional checks, not local propagated-accuracy estimates. Across 120 paired analyst interpretations, the P_2 RBW bias was 0.09 m, MAE was 0.45 m, RMSE was 0.83 m, and the Bland–Altman limits of agreement were −1.54 to 1.72 m. Non-negligible percentile sensitivity was also identified.

Orthorectified CCTV can complement intermittent terrestrial surveys by providing time-resolved horizontal beach-buffer observations. Further evaluation should prioritize denser checkpoints near the transects or a three-dimensional camera model, local water-level observations, directional wave spectra with validated nearshore transformation, and independent sites.

Author Contributions: Conceptualization, B.H. and K.K.; methodology, B.H.; software, B.H.; validation, M.S.; formal analysis, B.H.; investigation, G.K.; resources, G.K.; data curation, B.H.; writing—original draft preparation, B.H.; writing—review and editing, M.S.; visualization, B.H.; supervision, M.S. and G.K.; project administration, M.S. and K.K.; funding acquisition, K.K. All authors have read and agreed to the published version of the manuscript.

Funding: This work was supported by the Korea Institute of Marine Science and Technology Promotion (KIMST), funded by the Ministry of Oceans and Fisheries, Korea (RS-2023-00256687).

Data Availability Statement: The original contributions presented in this study are included in the article. Further inquiries can be directed to the corresponding author.

Conflicts of Interest: Authors Bohyeon Hwang, Minsuk Shin, Guenam Kim and Kihyon Kim were employed by the company GeoSystem Research Corp. All authors declare that the research was conducted in the absence of any commercial orfinancial relationships that could be construed as a potential conflictof interest.

Abbreviations

ADCP	Acoustic Doppler current profiler
CCTV	Closed-circuit television
CV	Coefficient of variation
GCP	Ground control point
IMSL	Incheon Mean Sea Level
MAE	Mean absolute error
NSE	Nash–Sutcliffe efficiency
RBW	Remaining beach width
RMSE	Root-mean-square error
RTK	Real-time kinematic
UAV	Unmanned aerial vehicle

Appendix A. CCTV Observation Periods Used for RBW Comparison

Table A1. Thirty-five CCTV observation periods assigned to the screened Q_{95} cohort are documented by the 53-candidate screening ledger. Wave-reference time is the actual hourly ADCP timestamp from which H_{m0}, T_p, and peak direction were taken for the Stockdon calculation. Peak direction is referenced to north, increases clockwise, and denotes the direction from which the waves approached.

No.	Wave-Reference Time (KST)	H_{m0} (m)	T_p (s)	Peak Direction, θ_p (°; Waves From)
1	16 December 2023, 09:00	2.24	10.27	66.18
2	17 December 2023, 10:00	2.20	10.46	49.81
3	22 December 2023, 16:00	1.75	9.66	48.30
4	1 January 2024, 13:00	2.15	10.11	38.61
5	13 January 2024, 13:00	1.60	7.76	43.66
6	15 January 2024, 11:00	2.42	10.28	51.52
7	19 January 2024, 10:00	2.31	8.90	51.14

Table A1. *Cont.*

No.	Wave-Reference Time (KST)	H_{m0} (m)	T_p (s)	Peak Direction, θ_p (°; Waves From)
8	20 January 2024, 10:00	2.43	7.20	54.84
9	23 January 2024, 14:00	2.89	11.35	57.27
10	24 January 2024, 14:00	3.40	12.10	57.73
11	25 January 2024, 08:00	3.55	13.07	65.98
12	26 January 2024, 17:00	2.36	11.91	64.70
13	27 January 2024, 12:00	2.32	12.41	68.27
14	1 February 2024, 17:00	2.70	9.11	52.98
15	5 February 2024, 15:00	2.93	8.78	73.18
16	15 February 2024, 17:00	2.64	8.93	46.34
17	11 March 2024, 10:00	2.36	12.01	332.28
18	20 March 2024, 12:00	1.92	9.34	71.96
19	22 March 2024, 18:00	1.69	5.76	141.00
20	25 March 2024, 17:00	1.84	6.13	81.09
21	26 March 2024, 17:00	2.03	8.19	97.53
22	9 April 2024, 10:00	1.96	7.34	66.25
23	8 May 2024, 07:00	1.89	11.56	73.86
24	26 November 2024, 10:00	2.54	8.34	136.83
25	19 December 2024, 07:00	1.69	8.60	79.86
26	11 January 2025, 11:00	1.83	13.14	87.86
27	25 January 2025, 09:00	2.01	7.41	86.25
28	2 February 2025, 14:00	1.73	8.11	87.49
29	8 February 2025, 16:00	1.67	9.97	74.97
30	3 March 2025, 09:00	3.01	7.76	71.01
31	4 March 2025, 18:00	2.86	8.38	93.02
32	5 March 2025, 07:00	2.19	9.04	87.78
33	28 March 2025, 18:00	1.68	8.68	50.48
34	24 May 2025, 16:00	1.69	7.26	88.10
35	25 May 2025, 07:00	2.00	8.56	77.79

Table A2. Twenty-five CCTV observation periods in the survey-matched cohort. Wave-reference time is the actual hourly ADCP timestamp used in the Stockdon calculation. Within each five-period survey group, the same local hour was used and aligned with the corresponding field-survey acquisition hour. Peak direction is referenced to north, increases clockwise, and denotes the direction from which the waves approached.

No.	Wave-Reference Time (KST)	H_{m0} (m)	T_p (s)	Peak Direction, θ_p (°; Waves From)
1	11 December 2023, 14:00	3.47	8.70	90.16
2	12 December 2023, 14:00	2.11	8.29	79.86
3	13 December 2023, 14:00	1.36	8.11	85.48
4	14 December 2023, 14:00	0.93	7.49	57.73
5	15 December 2023, 14:00	2.31	10.21	46.89
6	20 April 2024, 12:00	0.49	4.31	55.91
7	21 April 2024, 12:00	1.03	5.26	92.97
8	22 April 2024, 12:00	1.18	7.46	87.85
9	24 April 2024, 12:00	1.24	7.61	82.34
10	25 April 2024, 12:00	0.73	7.73	51.53
11	17 February 2025, 11:00	0.81	8.59	65.71
12	18 February 2025, 11:00	0.66	7.91	70.80
13	19 February 2025, 11:00	0.82	8.81	69.84
14	20 February 2025, 11:00	0.83	8.40	78.34
15	21 February 2025, 11:00	0.77	7.79	69.84
16	15 April 2025, 14:00	0.70	7.45	50.22

Table A2. *Cont.*

No.	Wave-Reference Time (KST)	H_{m0} (m)	T_p (s)	Peak Direction, θ_p (°; Waves From)
17	16 April 2025, 14:00	0.50	2.77	130.23
18	17 April 2025, 14:00	0.60	4.95	135.51
19	18 April 2025, 14:00	0.41	5.64	123.29
20	19 April 2025, 14:00	0.61	4.51	133.48
21	9 March 2026, 15:00	0.97	10.07	82.04
22	10 March 2026, 15:00	0.94	6.29	85.48
23	11 March 2026, 15:00	0.55	6.38	72.79
24	12 March 2026, 15:00	1.27	5.05	60.11
25	13 March 2026, 15:00	1.67	6.81	75.11

Table A3. CCTV observation periods used in the paired morphology-input timing sensitivity analysis. Actual hourly wave-reference times are shown together with the matched acquisition times for the five close surveys. Calendar-day offsets were used because sub-daily acquisition times were not archived consistently for all 11 candidate morphology surveys. Each period contributed two transect records; one closest morphology was within 5 calendar days, and the remaining 10 survey scenarios were at least 30 calendar days distant.

No.	Wave-Reference Time (KST)	Matched Survey Time (KST)	Calendar-Day Offset (d)	Distant Survey Count
1	11 December 2023, 14:00	13 December 2023, 14:00	2	10
2	12 December 2023, 14:00	13 December 2023, 14:00	1	10
3	13 December 2023, 14:00	13 December 2023, 14:00	0	10
4	14 December 2023, 14:00	13 December 2023, 14:00	1	10
5	15 December 2023, 14:00	13 December 2023, 14:00	2	10
6	16 December 2023, 09:00	13 December 2023, 14:00	3	10
7	17 December 2023, 10:00	13 December 2023, 14:00	4	10
8	20 April 2024, 12:00	22 April 2024, 12:00	2	10
9	21 April 2024, 12:00	22 April 2024, 12:00	1	10
10	22 April 2024, 12:00	22 April 2024, 12:00	0	10
11	24 April 2024, 12:00	22 April 2024, 12:00	2	10
12	25 April 2024, 12:00	22 April 2024, 12:00	3	10
13	17 February 2025, 11:00	19 February 2025, 11:00	2	10
14	18 February 2025, 11:00	19 February 2025, 11:00	1	10
15	19 February 2025, 11:00	19 February 2025, 11:00	0	10
16	20 February 2025, 11:00	19 February 2025, 11:00	1	10
17	21 February 2025, 11:00	19 February 2025, 11:00	2	10
18	15 April 2025, 14:00	17 April 2025, 14:00	2	10
19	16 April 2025, 14:00	17 April 2025, 14:00	1	10
20	17 April 2025, 14:00	17 April 2025, 14:00	0	10
21	18 April 2025, 14:00	17 April 2025, 14:00	1	10
22	19 April 2025, 14:00	17 April 2025, 14:00	2	10
23	9 March 2026, 15:00	11 March 2026, 15:00	2	10
24	10 March 2026, 15:00	11 March 2026, 15:00	1	10
25	11 March 2026, 15:00	11 March 2026, 15:00	0	10
26	12 March 2026, 15:00	11 March 2026, 15:00	1	10
27	13 March 2026, 15:00	11 March 2026, 15:00	2	10

References

1. Sallenger, A.H., Jr. Storm impact scale for barrier islands. *J. Coast. Res.* **2000**, *16*, 890–895.
2. Van der Meer, J.W.; Allsop, N.W.H.; Bruce, T.; De Rouck, J.; Kortenhaus, A.; Pullen, T.; Schüttrumpf, H.; Troch, P.; Zanuttigh, B. EurOtop: Manual on wave overtopping of sea defences and related structures. In *An Overtopping Manual Largely Based on European Research, but for Worldwide Application*, 2nd ed.; EurOtop: Leiden, The Netherlands, 2018.

3. Stockdon, H.F.; Holman, R.A.; Howd, P.A.; Sallenger, A.H., Jr. Empirical parameterization of setup, swash, and runup. *Coast. Eng.* **2006**, *53*, 573–588. [CrossRef]
4. Salmon, S.A.; Bryan, K.R.; Coco, G. The use of video systems to measure run-up on beaches. *J. Coast. Res.* **2007**, *50*, 211–215. [CrossRef]
5. Vousdoukas, M.I.; Wziatek, D.; Almeida, L.P. Coastal vulnerability assessment based on video wave run-up observations at a mesotidal, steep-sloped beach. *Ocean Dyn.* **2012**, *62*, 123–137. [CrossRef]
6. Di Luccio, D.; Benassai, G.; Budillon, G.; Mucerino, L.; Montella, R.; Pugliese Carratelli, E. Wave run-up prediction and observation in a micro-tidal beach. *Nat. Hazards Earth Syst. Sci.* **2018**, *18*, 2841–2857. [CrossRef]
7. Stockdon, H.F.; Long, J.W.; Palmsten, M.L.; Van der Westhuysen, A.; Doran, K.S.; Snell, R.J. Operational forecasts of wave-driven water levels and coastal hazards for US Gulf and Atlantic coasts. *Commun. Earth Environ.* **2023**, *4*, 169. [CrossRef]
8. Serafin, K.A.; Ruggiero, P. Simulating extreme total water levels using a time-dependent, extreme value approach. *J. Geophys. Res. Oceans* **2014**, *119*, 6305–6329. [CrossRef]
9. Didier, D.; Bernatchez, P.; Boucher-Brossard, G.; Lambert, A.; Fraser, C.; Barnett, R.L.; Van-Wierts, S. Coastal flood assessment based on field debris measurements and wave runup empirical model. *J. Mar. Sci. Eng.* **2015**, *3*, 560–590. [CrossRef]
10. Ruggiero, P.; Holman, R.A.; Beach, R.A. Wave run-up on a high-energy dissipative beach. *J. Geophys. Res.* **2004**, *109*, C06025. [CrossRef]
11. Doran, K.S.; Long, J.W.; Overbeck, J.R. *A Method for Determining Average Beach Slope and Beach Slope Variability for U.S. Sandy Coastlines*; U.S. Geological Survey Open-File Report 2015-1053; U.S. Geological Survey: Reston, VA, USA, 2015; 5p. [CrossRef]
12. Park, H.; Cox, D.T. Empirical wave run-up formula for wave, storm surge and berm width. *Coast. Eng.* **2016**, *115*, 67–78. [CrossRef]
13. Poate, T.G.; McCall, R.T.; Masselink, G. A new parameterisation for runup on gravel beaches. *Coast. Eng.* **2016**, *117*, 176–190. [CrossRef]
14. van Ormondt, M.; Roelvink, D.; van Dongeren, A. A model-derived empirical formulation for wave run-up on naturally sloping beaches. *J. Mar. Sci. Eng.* **2021**, *9*, 1185. [CrossRef]
15. Lippmann, T.C.; Holman, R.A. Quantification of sand bar morphology: A video technique based on wave dissipation. *J. Geophys. Res.* **1989**, *94*, 995–1011. [CrossRef]
16. Kroon, A.; Davidson, M.A.; Aarninkhof, S.G.J.; Archetti, R.; Armaroli, C.; Gonzalez, M.; Medri, S.; Osorio, A.; Aagaard, T.; Holman, R.A.; et al. Application of remote sensing video systems to coastline management problems. *Coast. Eng.* **2007**, *54*, 493–505. [CrossRef]
17. Holman, R.A.; Stanley, J. The history and technical capabilities of Argus. *Coast. Eng.* **2007**, *54*, 477–491. [CrossRef]
18. Almar, R.; Blenkinsopp, C.; Almeida, L.P.; Cienfuegos, R.; Catalán, P.A. Wave runup video motion detection using the Radon Transform. *Coast. Eng.* **2017**, *130*, 46–51. [CrossRef]
19. Buckley, M.L.; Buscombe, D.; Birchler, J.J.; Palmsten, M.L.; Swanson, E.; Brown, J.A.; Itzkin, M.; Storlazzi, C.D.; Harrison, S.R. Wave runup and total water level observations from time series imagery at several sites with varying nearshore morphologies. *Coast. Eng.* **2024**, *193*, 104600. [CrossRef]
20. Shirai, T.; Arikawa, T. Automated wave runup monitoring using coastal CCTV cameras for tsunami detection. *Sci. Rep.* **2025**, *15*, 44429. [CrossRef] [PubMed]
21. Otsu, N. A threshold selection method from gray-level histograms. *IEEE Trans. Syst. Man Cybern.* **1979**, *9*, 62–66. [CrossRef]
22. Nash, J.E.; Sutcliffe, J.V. River flow forecasting through conceptual models, Part I: A discussion of principles. *J. Hydrol.* **1970**, *10*, 282–290. [CrossRef]